Journal of the European Ceramic Society 44 (2024) 116743

Contents lists available at ScienceDirect

Journal of the European Ceramic Society

journal homepage: www.elsevier.com/locate/jeurceramsoc

$CuMn_{1.7}Fe_{0.3}O_4$ – RE_2O_3 (RE = Y, Gd) bilayers as protective interconnect coatings for solid oxide cells

Bartłomiej Lemieszek [a,*], Justyna Ignaczak [a], Krystian Lankauf [a], Patryk Błaszczak [b], Maciej Bik [c], Marcin Zając [d], Maciej Sitarz [c], Piotr Jasiński [a], Sebastian Molin [a]

[a] Advanced Materials Center, Faculty of Electronics, Telecommunications and Informatics, Gdańsk University of Technology, ul. G. Narutowicza 11/12, Gdańsk 80-233, Poland
[b] Advanced Materials Center, Faculty of Applied Physics and Mathematics, Gdańsk University of Technology, ul. G. Narutowicza 11/12, Gdańsk 80-233, Poland
[c] AGH University of Science and Technology, Faculty of Materials Science and Ceramics, Al. Mickiewicza 30, Kraków 30-059, Poland
[d] National Synchrotron Radiation Centre SOLARIS, Jagiellonian University, Czerwone Maki 98, Kraków 30-392, Poland

ARTICLE INFO

Keywords:
High temperature corrosion
Solid oxide cell (SOC)
Bilayers
Protective coating
Reactive element effect

ABSTRACT

Efficient replacement of materials based on critical elements such as cobalt is one of the greatest challenges facing the field of solid oxide cells. New generation materials, free of cobalt show potential to replace conventional materials. However, these materials are characterised by poor ability to block chromium diffusion. This article described the study of $CuMn_{1.7}Fe_{0.3}O_4$ (CMFO) spinel combined with single metal oxide (Y_2O_3 or Gd_2O_3) thin films as protective coatings for steel interconnects. CMFO was examined using XRD and TPR. Coated steel samples were oxidised in an air atmosphere at 700 °C for 4000 h. The coatings and oxide scale microstructures and cross-sections were examined by CRI, XRD, and SEM-EDX. The electrical properties of the steel-coating system were evaluated using Area Specific Resistance measurements. Based on the results obtained, it can be concluded that the use of thin layers of rare earth oxides allowed for better blocking of chromium diffusion.

1. Introduction

High-temperature corrosion of steel interconnects is one of the main degradation problems in solid oxide cell stacks. At high temperatures, ferritic steels develop a chromium oxide scale, which further protects the steel substrate from uncontrolled oxidation [1,2]. The thickness of the chromium oxide layer increases with time according to parabolic oxidation kinetics [3]. Oxide growth causes two important factors: an increase in the electrical resistance (area specific resistance – ASR) and the evaporation of chromium (at air side), reducing the efficiency of the fuel cells [1,2,4]. One of the mitigation strategies is to coat the interconnects with dedicated protective coatings. Various materials have been considered for coating ferritic steels, including metallic coatings [5–8], reactive element oxides [9–18], perovskite oxides [1,19–26], and spinels [27–34]. Among these materials, reactive-element oxides and spinels are particularly often used.

Reactive-element oxides in the form of La_2O_3, CeO_2, Gd_2O_3, and Y_2O_3 are used commonly as coatings or additives for high temperature alloys and also were successfully used to coat interconnects. These materials are characterised by a high affinity for oxygen, blocking the diffusion of chromium to the surface of the layer, and increasing the adhesion of the layer to the metallic substrate [1]. The main disadvantage of this group of ceramics is limited electronic conductivity, therefore the coating thicknesses are usually low, below ~ 1 μm [9]. Yoon et al. described the application of La_2O_3 as a coating of STS444 interconnects (stainless steel). The study examined the surface morphology and cross-sections after 500 h at 700 °C. The presence of phases such as Cr_2O_3, $LaCrO_3$, and $(Mn,Cr)_3O_4$ was demonstrated [14]. Molin et al. used thin Y_2O_3 coatings of a thickness below 100 nm on Crofer 22 APU and tested the protective properties of the layer on the steam-hydrogen side at 750 °C for 2000 h. The described thin-layer coating resulted in a reduction in the thickness of the oxide layer and a high and stable ASR value over time [10]. Lemieszek et al. demonstrated the influence of thin layers (CeO_2, Gd_2O_3, La_2O_3, Y_2O_3—thickness below 100 nm) on Crofer 22 APU steel in an air atmosphere at 700 °C for 2000 h. It has been shown that the use of coatings reduces significant weight gain, especially in the case of La_2O_3 and Y_2O_3 coatings. The best ASR values were demonstrated by samples with a Gd_2O_3 or Y_2O_3 coating [18]. These coatings, even though they reduce oxide scale growth kinetics, they do not prevent Cr-diffusion and

* Corresponding author.
E-mail address: bartlomiej.lemieszek@pg.edu.pl (B. Lemieszek).

https://doi.org/10.1016/j.jeurceramsoc.2024.116743
Received 10 May 2024; Received in revised form 22 June 2024; Accepted 10 July 2024
Available online 11 July 2024

evaporation, as the external surface remains as Cr_2O_3, just with a lowered thickness.

As $MnCo_2O_4$ (MCO) spinel is the current state-of-the-art protective layer for SOC metallic interconnects. This material was found to be highly effective at preventing oxidation and reducing chromium diffusion and evaporation in metallic interconnects [35]. The focus is now aimed towards finding alternative materials than MCO. The cost and difficult working conditions of mining cobalt, as well as its carcinogenicity, cannot be overlooked [36,37]. That is why materials substituting cobalt with, e.g., copper have been developed, with various dopants [32–34]. For example, Ignaczak et al. synthesised a new spinel material, $Mn_{1.7}Cu_{1.3-x}Fe_xO_4$ (x = 0, 0.1, 0.3, 0.5) [38] and $Mn_{2-x}CuFe_xO_4$ (x = 0.0, 0.1, 0.3) [39], using a modified Pechini method.

The structure of the $Mn_{1.7}CuFe_{0.3}O_4$ after synthesis and calcination at 400 °C reveals the presence of the main phase being $CuMn_{1.7}Fe_{0.3}O_4$ with a mixed cubic (*Fd-3m*) and a tetragonal (*I41/amd:2*) spinel structure. Following the increase in Fe doping, the size of the unit cell was reduced. Additional CuO phases were not detected when annealing spinel at temperatures higher than 400 °C. [38]. Mazur et al. denoted a conductivity of 106 S cm^{-1} for $Cu_{1.15}Mn_{1.55}Fe_{0.3}O_4$ at 800 °C when the material was synthesised by the EDTA-gel process [40]. Hosseini et al. described the coating of AISI 430 steel with a layer of $Cu_{1.3}Mn_{1.7}O_4$ spinel, and the corrosion properties were examined at 750 °C for 500 h. A 70 % reduction in the ASR value was observed from 63.5 to 19.3 mΩ cm^2 at 750 °C. It was also observed that the oxide layer formed after the oxidation process was ~ 4 μm [41]. Study by Ignaczak et al. showed several beneficial features of the Mn-Cu based oxide spinels over the Mn-Co based oxide spinels: higher electrical conductivity, especially ≤ 700 °C, well matched thermal expansion coefficient. The drawback has been lower intrinsic oxidation protection, i.e. the steels coated with MCO showed lower weight gain in comparison to the Mn-Cu based oxide spinels coated steels [39].

A new trend is the coating of interconnects with double layers, most often in the form of a thin layer of a reactive element oxide and a thicker layer of spinel, but also double layers based of perovskite oxides [42,43]. The concept of coating interconnects with two materials is to use the advantages of each type of material. The use of a RE-oxide in combination with spinels makes use of the advantages of each material. Balland et al. presented the results of an investigation on the coating of interconnects with lanthanum oxide and $(Co,Mn)_3O_4$ on Crofer APU steel for a maximum of 1000 h at 800 °C. Coating involved applying lanthanum oxide and annealing for 100 h then depositing metallic (Co, Mn). This ultimately resulted in the formation of $La(Cr_{1-x}Mn_x)O_3$ and $(Co,Mn)_3O_4$ layers [17]. Brylewski et al. examined the influence of a double layer composed of Gd_2O_3 and $MnCo_2O_4$. The RE-oxide layer was applied by spin coating and the spinel layer by electrophoretic deposition. The samples were fired at 800 °C for 2260 h in an airtight atmosphere. An effective reduction in the formation of volatile chromium compounds and a significant reduction in weight gain and area-specific resistance were found [44]. Mazur et al. presented the results of coating Crofer 22 APU steel with a double layer composed of Gd_2O_3 and $MnCo_2O_4$. Thermogravimetric tests were performed at 800 °C for 7000 h. A significant reduction in weight gain and a very low ASR value of 0.019 Ω cm^2 after the final stage of oxidation were demonstrated. Tests were also carried out using a fuel cell to check the ability of the protective layers to block the formation of active chromium species that could poison the cell's cathode. This study clearly indicated the effective blocking of this element by the combination of materials used as protective layers [45]. To the best of our knowledge, there is no mention in the literature of the use of bi-layer coating in the form of reactive element oxide and spinel $(CuMnFe)_3O_4$.

This research work presents the results of coating Crofer 22 APU steel with bi-layers of RE-oxide (yttrium oxide or gadolinium oxide) and a top layer of $CuMn_{1.7}Fe_{0.3}O_4$ spinel. The selection of these two RE-oxides is based on conclusions from previous studies due to the reduction in weight gain and lower ASR values [18]. The samples were tested via thermogravimetric measurements in isothermal conditions for a 4000 h. Post-mortem analysis was used to study and compare the structural properties of the materials using methods such as XRD, SEM-EDS, XAS spectra, and Confocal Raman imaging. Additionally, the electrical properties of the samples were tested.

2. Materials and methods

2.1. RE-oxide layer deposition

The base solution used to obtain the RE-oxide layers was 2 mM Gd $(NO_3)_3$•$6H_2O$ (Sigma Aldrich 99.9 % purity, USA) or $Y(NO_3)_3$ • $6H_2O$ (Sigma Aldrich 99 % purity, USA) dissolved in ethanol (Sigma Aldrich 99.8 %, USA). For rare earth oxide electrolytic deposition, substrates of 1.5 × 1.5 cm^2, 0.3 mm thick plates were cut from Crofer 22 APU steel (VDM Metals, Germany). A small hole (3 mm in diameter) was punched in the upper part of the samples. Noticeable flexures were removed from the edges of the plates using a polishing machine with wet 1200 grit paper. Before applying the rare earth yttrium or gadolinium oxide coatings (attributed as RE further in the text), the plates were meticulously cleaned in an ultrasonic bath containing a solution of distilled water, then in acetone (POCH, Poland). Crofer 22 APU steel plate was used as the working electrode (cathode) in a two-electrode electrolytic deposition system. Crocodile clips were used to connect to the cleaned and dried plates. The counter electrode (anode) was a large Crofer 22 APU steel sheet positioned symmetrically on either side of the working electrode (active geometric surface area of about 50 cm^2). The distance between the working and counter electrodes was less than 15 mm.

A programmable power supply was used to apply 40 V between the electrodes (Delta Elektronika Power supply SM 300-5, The Netherlands). Based on a previous study, the deposition time was selected as 1 min (thickness ~ 100 nm) [18]. After applying the RE layer, each sample was air-dried and heated to 400 °C to ensure the complete conversion of the deposited layers to oxides and the breakdown of residual nitrates.

2.2. Spinel synthesis and deposition

$Cu(NO_3)_2$ • $2.5H_2O$ (Sigma Aldrich, 99.999 % purity, USA), $Mn(NO_3)_2$ • $4H_2O$ (Sigma Aldrich, 97 % purity, USA), and $Fe(NO_3)_3$ • $9H_2O$ (Sigma Aldrich, 99.999 % purity, USA) were dissolved in distilled water and used as the starting solutions. According to the intended nominal composition of the spinel powders, those were mixed in proper molar ratio. The solutions were heated to 80 °C with constant stirring on a heating plate equipped with a magnetic stirrer. Citric acid ($C_6H_8O_7$, Sigma Aldrich, 99 % purity, USA) and EDTA ($[CH_2N(CH_2COOH)_2]_2$, Sigma Aldrich, 99 % purity, USA) were added to the stirred solution in a molar ratio of 2:1:1-TMI as chelating agents (TMI – total number of molar ions). Diluted ammonia (25 w/w% H_2O) was added dropwise to adjust the pH to 9. To initiate the transesterification process, ethylene glycol ($C_2H_6O_2$, 98 % purity, Saint Louis, USA) was added while stirring constantly in an amount sufficient to obtain a ratio of 1 mol polyalcohol to 1 mol metal cations. The liquid precursor was maintained at 80 °C until a dense gel-like structure was achieved. The resultant gel was placed in a muffle furnace and heated to 400 °C for two hours. After this, the obtained powder was fired at 800 °C for 2 h. To achieve the lowest possible grain size, the powder was ball milled using the roll mill method with zirconia milling balls (Ø = 3 mm) and a rotational speed of 800 rpm for 4 h using a planetary mill.

The $CuMn_{1.7}Fe_{0.3}O_4$ (CMFO) spinel layer was applied by the electrophoretic deposition technique using Crofer 22 APU steel as the cathode (identical to the RE-oxide layer) with the same dimensions. The anode was Crofer 22 APU steel with a larger surface area (50 cm^2). The base solution contained 1 g of CMFO powder dispersed in isopropanol: acetone (4:1 ratio, 100 ml). Crystalline iodine (0.1 g per 100 ml of solution) was added to the solution. The resulting mixture was sonicated in an ultrasonic bath for 15 min to disperse the spinel particles in the

liquid. Three types of samples were prepared. The first type was Crofer 22 APU steel samples with only the spinel layer (labelled as 'CMFO'). The second type consisted of samples with a thin layer of gadolinium oxide and, on top of that, a spinel layer (labelled as 'CMFO-Gd_2O_3'). The last type was samples with an yttrium oxide layer (same thickness) and the spinel layer (labelled as 'CMFO-Y_2O_3'). Uncoated Crofer 22 APU steel plates were used as reference samples (labelled as 'reference'). The summary of the prepared samples is presented in Table 1. A programmable power supply (Delta Elektronika Power Supply SM 300-5, The Netherlands) was used to apply 80 V between the electrodes. The duration of the electrophoresis was 4 minutes to obtain a spinel layer of ~ 10 μm thickness. After coating the steel, a heat treatment process was applied under a reducing and oxidising atmosphere. The reduction step was carried out in tube furnace (Carbolite STF 16/450, Germany) at 800 °C for 10 h under a hydrogen atmosphere with a flow 175 ml min^{-1}, and an oxidation step at 900 °C for 2 h under air in a box furnace (Linn High Therm LM412.05, Germany). The selection of these conditions was based on preliminary tests determining the optimal conditions, and the choice of a lower temperature was associated with the result of smaller metallic particles of copper and iron. The use of a lower temperature for the reduction stage also reduces the thickness of the chromium oxide layer after the oxidation stage.

2.3. Measurements methods

Temperature-programmed reduction (TPR) test was performed for $CuMn_{1.7}Fe_{0.3}O_4$ using an in-house-built TPx unit including a TCD (Buck Scientific, USA), heated transfer line, and specially designed quartz reactor. For the reduction test, 75 mg of spinel powder was placed in the reactor. Quartz wool was used to create a homogeneous reactive bed and limit the elution of the powder. The TPR test was performed under the standard 5 vol% H_2 in Ar and flow rate of 40 ml min^{-1}. The sample was heated up from room temperature to ~ 900 °C at a rate of 10 °C min^{-1} with the data collection frequency set to 1 Hz. The sample of $CuMn_{1.7}Fe_{0.3}O_4$ underwent two following cycles of reduction interspersed with the collection of the oxidation profile under the same experimental conditions, although under a stream of 5 % O_2/He reactive gas. For comparison, a sample of commercial $MnCo_2O_4$ powder (Marion Technologies, France) was measured while under reduction.

X-ray diffraction (XRD) was used to examine the microstructure of the coated Crofer 22 APU steel samples using a Bruker D2Phaser (Bruker AXS, Germany) diffractometer with a Lynxeye XE-T detector and CuKα radiation (λ = 0.15406 nm). XRD measurements of the synthesised powder were made for the powder after treatment at 800 °C under atmospheric air and for prepared samples after 1000 h, 2000 h and 4000 h of oxidation.

To determine the oxidation kinetics, the samples were subjected to a temperature of 700 °C under an air atmosphere in a box furnace (Nabertherm L9/11/B180, Germany). The weight gain was measured using a balance with a precision of 10^{-6} grammes (Radwag XA 6/21Y.M. A.B PLUS, Poland). The 'long-term' corrosion study was carried out for 4000 h in 250-hour cycles (16 cycles), followed by mass measurement and calculation of the mass increase. For each of the sample types, 16 specimens were assigned for long-term testing, of which 3 samples were taken out after 1000 h, 4 after 2000 h, and the remaining 9 were removed after the final period of 4000 h. Uncoated Crofer 22 APU steel was used as a reference sample (5 samples). As for the coated samples, one reference sample was taken out after 1000 h, two after 2000 h and two after 4000 h.

Electrical resistance measurements were performed ex-situ for samples after oxidation times equal to zero, 1000, 2000, and 4000 h. As a reference, uncoated samples that had undergone the same oxidation times were used. In a cross-scale setup, electrical resistance tests were conducted (Pt/layers/steel/layers/Pt). On both sides of the steel, platinum electrodes (with a surface area of 0.5 cm^2) were painted with a brush, dried, and heated at 700 °C for two hours. The electrical resistance was measured using an impedance analyser in a four-electrode setup (Vertex.5A, Ivium Technologies, The Netherlands). The test was performed at a frequency of 1 Hz with an amplitude of 1 mA (the imaginary component of the impedance was negligible). The samples were heated to 700 °C, and the resistance was measured in a cooling cycle every 50 °C down to 300 °C. The maximum current density through the specimen was restricted to 10 mA cm^{-2}.

Cross-sections and the steel surface with a protective layer were examined using scanning electron microscopy (SEM) on a stationary SEM Phenom XL (Thermo Fisher Scientific, USA) at an accelerating voltage of 15 kV and a pressure of 0.1 Pa. A SED (secondary electron detector) and integrated energy dispersive X-ray microanalyser (EDX) were used. The samples were imbedded in epoxy resin (EpoFix, Struers) and then polished to a 1 μm finish using a semi-automatic Struers Tegramin-20 machine. Prior to the imaging step, the samples were sputtered with a thin carbon layer for better charge transfer and higher resolution of the SEM images.

Raman spectroscopy (Raman Confocal imaging) was carried out using a WITec alpha 300 M+ spectrometer (488 nm laser line). Measurements were carried out on pre-prepared cross sections, using a 100 × ZEISS Epiplan-Neofluar objective with NA = 0.9 and 600 grating (spectral resolution of ca. 3 cm^{-1}). The areas of a constant width (5 μm) were scanned and their height (from 8 to 13 μm) was dependent on scale/coating thickness. The integration time for a single spectrum was equal to 15 s. The WITec Control FIVE software was used to record Raman spectra, whereas WITec Project FIVE 5.3 PLUS, as well as the OPUS 7.2 software were used to post-process and analyse the results. Prior to analysis, preliminary mathematical processing – extracting the desired range (115–1000 cm^{-1}), baseline correction and cosmic spikes removal (the CRR filter) – was executed. Subsequently, an integration filter (with both specific position and width on the spectrum) was applied to the characteristic spectral regions (e.g. the Cr_2O_3 band at ca. 555 cm^{-1}). As a result, chemical distribution maps were generated, a set of distribution images was revealed, and the most representative spectra for each phase were extracted manually, which determined the presence of dominating phases.

X-ray Absorption Spectroscopy (XAS) was performed using the PIRX beamline at the SOLARIS National Synchrotron Radiation Centre, Kraków, Poland. The spectra were collected for various compositions of the prepared protective coating as well as the samples subjected to different oxidation times. Measurements were made for all three elements included in the analysed material by measuring the absorption spectra at the L_3 and L_2 edges of Cu, Mn, and Fe. In the case of copper, pure, and high-grade oxides of Cu_2O and CuO were used as the reference. For manganese, MnO oxide, Mn_2O_3, and MnO_2 oxides were taken as nominal materials. Fe_3O_4 oxide was used to determine the iron oxidation state in the prepared samples.

3. Results

3.1. Powder preparation and characterisation

The phase composition of the powders was determined by XRD measurements. The obtained diffraction pattern for the $CuMn_{1.7}Fe_{0.3}O_4$

Table 1
Nomenclature division of samples with different types of protective layers.

Sample name	Reference	CMFO	CMFO-Gd_2O_3	CMFO-Y_2O_3
Sample composition	Bare Crofer 22 APU	$CuMn_{1.7}Fe_{0.3}O_4$	$CuMn_{1.7}Fe_{0.3}O_4$ – Gd_2O_3	$CuMn_{1.7}Fe_{0.3}O_4$– Y_2O_3

powder is presented in Fig. 1A. Peaks were observed for the cubic phase (space group: *Fd-3m*) at 17°, 31°, 36°, 37.5°, 43°, 52°, 54°, 58°, 64°, and 75°, and for the tetragonal phase (space group: *I41/amd:2*) at 32°, 45°, and 65°. Impurities in the form of MnO_2 and Mn_3O_4 oxide were also observed. Peaks corresponding to MnO_2 were found at 29°, 37°, 57°, 59°, 61°, and 65° and for Mn_3O_4 at 18°, 31°, 44°, and 65°. Ignaczak et al. also observed a mixed cubic and tetragonal phase occurring for $Mn_{1.7}CuFe_{0.3}O_4$ [38]. Bobruk et al. observed $Cu_{1.3}Mn_{1.7}O_4$ impurities in the form of Mn_2O_3 [46].

Due to the requirement of sintering of the spinel-based coatings in reducing-oxidising conditions (redox sintering), understanding the spinel reduction process can be valuable [47]. TPR profiles can indicate the reducing reactivity of metal oxides. In general, a decrease in the reduction temperature indicates an increase in the reduction activity. The composition, particle size and surface area of the metal oxide influence its reducing capacity. The resulting reduction profiles of the spinel are presented in Fig. 1B. Two reduction cycles were performed to better understand the processes happening during the coating preparation step. Two main reduction regions (peaks) were observed, which describe the processes taking place in a complex way. At a temperature close to ~ 250 °C, the start of the reduction of the Cu^{2+} is visible (α), which is quite common in the field of Cu-based spinels. The Cu ions are being easily reduced to Cu^{+} and further into metallic form, which is quite a fast process with no clear distinction between the two steps [48]. The reduction process of Cu ions, depending on the degree of doping, can take place up to a temperature of 400 °C. In this case, it seems to overlap with the manganese ions reduction signal when reducing Mn^{4+} to Mn^{3+} at around 306 °C (β) [49].

Lower temperatures of the reduction into purely metallic species are characteristic for CuO deposited onto carriers such as YSZ or ZrO_2, as well as for highly dispersed copper oxide and Cu^{2+} cations in the octahedral structure of the materials [50–55]. The β peak is a superposition of the single-step bulk Cu^{2+} reduction and the first Mn reduction step. The manganese reduction process from Mn^{4+} to Mn^{2+} revealed a first maximum at ~ 306 °C and continues as a two-step process up to 365 °C (γ) when most of the Mn ions are being converted into a Mn^{2+} state, forming a precipitate of MnO. The lowering of the Mn reduction temperature can be attributed to the Cu-induced spillover effect [56]. Metallic Cu particles are increasing the kinetics of the reduction process of the bulk spinel and the coating preparation temperature can be lowered. The aforementioned processes are also overlapping with the reduction of $Fe^{4+/3+}$ ions into $Fe^{3+/2+}$ species, also indicated as the γ peak. After that step, the sample still contains the Fe_3O_4-FeO phase, which upon further heating above 600 °C under H_2, is slowly converted into metallic iron [55,57–59]. The reduction of iron above 600 °C does not have such a large impact due to the low content of this element in the material. Following the reduction of the spinel structure, it is decomposed into the corresponding mixture of separated oxides/metals. The formation of metallic manganese is not possible within the analysed temperature/pO_2 range and the sample is composed of MnO mixed with metallic Cu and FeO/Fe. The oxidation profile is shown in Fig. S1 A and indicates that full reoxidation was finished up to 800 °C with visible maxima coming from each of the substituents found in the reduced sample. The secondary reduction profile visible in Fig. 1B shows that after the reduction and oxidation process, the spinel structure seems to become more homogenous and most likely tends to recrystallise into micrometric grains, that due to the overwhelming amount of Cu is being reduced in one step with no clear distinction between the undergoing processes. One should take that into account when performing the reduction process, as too-rapid structural changes might induce huge internal stresses and may lead to lower integrity of the layer. Fig. S1 B shows the reduction profile of $MnCo_2O_4$ (MCO) spinel. Compared to the MCO spinel, most of the reduction process of $CuMn_{1.7}Fe_{0.3}O_4$ takes place at temperatures lower than for MCO. For MCO, the main peaks corresponding to the reduction of Co and Mn species to metallic Co and MnO were located at 500 and 685 °C. The result is in line with previous reports on the MCO reduction behaviour [60]. Disregarding the sluggish reduction of the FeO down to metallic Fe, the $CuMn_{1.7}Fe_{0.3}O_4$ is more easily reducible. The reason for such recognition of peaks in TPR is to take into account the value of the redox potential of each cation and to take into account literature data. The redox potentials are respectively for the conversion from $\varphi MnO_2/Mn^{2+}$, $\varphi Mn^{3+}/Mn^{2+}$: + 1.224 eV and + 1.51 eV, respectively, ($\varphi Mn^{2+}/Mn^{0}$) is − 1.186 eV; $\varphi Fe^{3+}/Fe^{2+}$, $\varphi Fe^{2+}/Fe^{0}$ are + 0.771 eV and − 0.44 eV, respectively. The redox potential for copper reduction Cu^{2+}/Cu^{0} is + 0.342 eV.

3.2. Oxidation test

The influence of the spinel layer on steel corrosion behaviour and the influence of a thin ceramic layer of gadolinium oxide and yttrium oxide were investigated by subjecting the samples to corrosion tests at 700 °C. Those conditions were chosen based on the current temperature trend in the SOC [61].

The results of the cyclic thermogravimetry measurements are shown in Fig. 2A in a linear scale, in 2B in a parabolic scale, and in 2 C, the variation of the instantaneous corrosion rate over the course of the experiment. In the case of long-term corrosion, the highest weight gain was observed for the reference sample, equal to 0.158 ± 0.009 mg cm^{-2} after 4000 h. However, a slowdown in the increase in weight gain is visible after 3000 h, where the weight change is small, and after 3500 h, the mass is being maintained practically constant. For the CMFO samples, the total weight gain after 4000 h was 0.042 ± 0.005 mg cm^{-2},

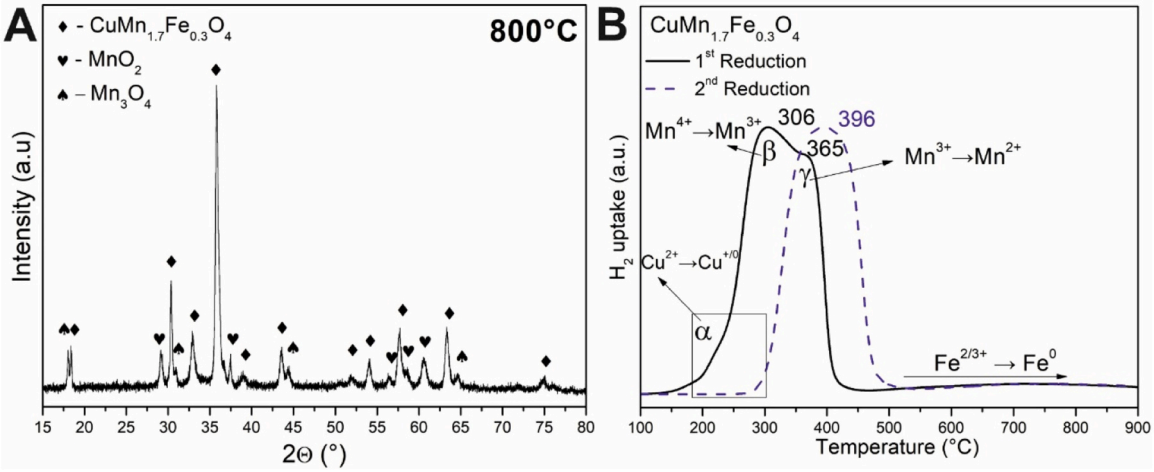

Fig. 1. XRD of the $CuMn_{1.7}Fe_{0.3}O_4$ spinel after calcination at 800 °C (A) and the TRP plot for the reduction of the $CuMn_{1.7}Fe_{0.3}O_4$ (B).

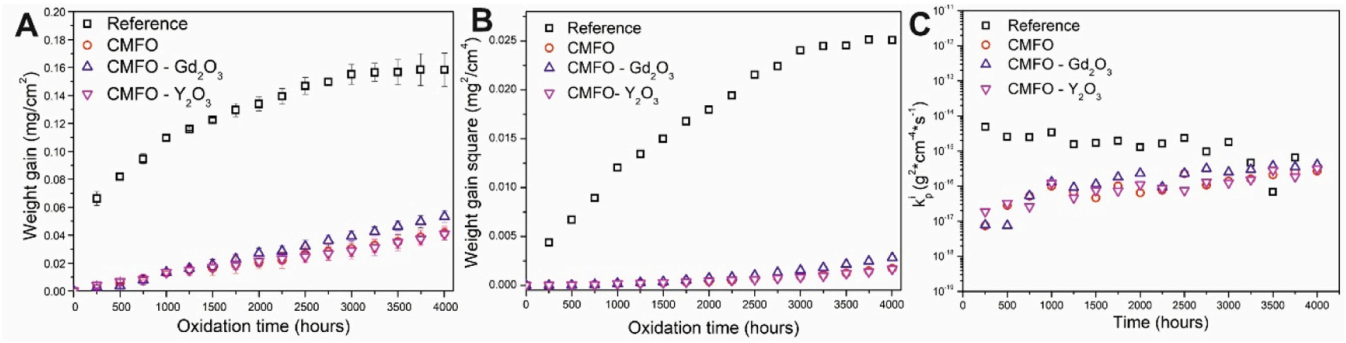

Fig. 2. Weight gain plots for long-term corrosion tests (a), parabolic plot (b), and calculated instantaneous k_p values (c).

which was more than a threefold decrease in this value compared to the reference sample. The same was observed with the CMFO-Gd_2O_3 samples, where after 4000 h, an increase in mass was equal to 0.053 ± 0.004 mg cm^{-2} was seen. The lowest weight gain was obtained for the CMFO-Y_2O_3 samples. Samples with a yttria layer and spinel showed a weight gain after 4000 h equal to 0.041 ± 0.004 mg cm^{-2}, i.e., nearly four times less weight gain than the reference sample.

For clarity, Fig. S2 A and B shows weight gains of coated samples excluding the reference sample. Values presented in Figs. 2 and S2 are based on the average weight gain of the samples. Fig. S3 shows the individual weight gains of the tested specimens of CMFO (S3 A), CMFO-Gd_2O_3 (S3 B) and CMFO-Y_2O_3 (Fig. S3 C). All samples showed a similar variation in weight gain values. However, for the CMFO samples, a smaller number of samples was included in the average due to the occurrence of the layer detaching during the oxidation. This may be influenced by a slightly different TEC (thermal expansion coefficient) which for MCO is 13.1 10^{-6} K^{-1} and for spinel $Cu_{1.4}Mn_{1.6}O_4$ it was set at 13.9 10^{-6} K^{-1} [62,63]. For Crofer 22 APU steel, this value was defined as ~ 12 10^{-6} K^{-1} [63].

The obtained results were compared with other results for similar materials obtained by other groups. Talic et al. showed that Crofer 22 APU steel coated with an MCO protective layer showed a weight gain after 4000 h of a little over 0.08 mg cm^{-2}. Higher weight gains were observed for MCO doped with iron and copper, with ~0.10 mg cm^{-2} and ~ 0.12 mg cm^{-2} in that study [29]. Mazur et al. described a weight gain close to 0.1 mg cm^{-2} [40] for samples of Nirosta 4016/1.4016 steel coated with spinel $Cu_{1.25}Mn_{1.65}Ni_{0.1}O_4$ and oxidised at 800 °C for 2000 h. In their work, Ignaczak et al. compared the weight gains of Crofer 22APU steel samples coated with iron-doped Mn_2CuO_4, $Mn_{1.9}CuFe_{0.1}O_4$, $Mn_{1.7}CuFe_{0.3}O_4$, and MCO, a reference sample (steel sample), and a reference sample of pre-oxidised steel. The smallest mass increase was found in samples with an MCO layer, then pre-oxidised, and subsequently $Mn_{1.7}CuFe_{0.3}O_4$, $Mn_{1.9}CuFe_{0.1}O_4$, and Mn_2CuO_4. The oxidation was carried out at 750 °C for 3000 h [39]. Talic et al. tested the MCO coating of Crofer 22H, 441, and 430 steel, and the corrosion properties were analysed at 700 °C. The corrosion time was 2000 h. The obtained weight gain values at the final stage of the experiment were approximately 0.081 mg cm^{-2}, 0.003 mg cm^{-2}, and − 0.031 mg cm^{-2} for steel 441, 430, and Crofer 22H, respectively. The weight gain measurements were subject to considerable error, as indicated by the error bars. A weight loss was observed for Crofer 22H steel coated with MCO. In the case of 430 steel, a reduction in weight gain was initially observed. Then, an increase in mass was observed, and at the final stage of the experiment, the mass increase was higher than the initial value. This problem did not occur in the case of steel 441; however, the weight gain values were very close to the values for steel without a protective layer [64]. The cited literature data indicate good anti-corrosion properties. All the quoted weight gain values are higher than those obtained in this work. The only lower mass increases were observed in the work where it was difficult to analyse mass increases at such low temperatures. In this work, this effect was also improved by using a thin layer of RE-oxide.

The kinetics of the oxidation reaction at high temperatures is described by the square dependence of the weight change during oxidation. The parabolic law is described by the equation:

$$\left(\frac{\Delta m}{A}\right)^2 = k_p t + C \quad (1)$$

where: Δm is the weight gain (g), A is the sample area (cm^2), k_p is the parabolic rate constant (g^2 cm^{-4} s^{-1}), t is the oxidation time (s), and C is the integration constant (g^2 cm^{-4}) [65]. The calculated values of the k_p coefficient are shown in Table 2. The analysed oxidation time was divided into 3 stages (0–1000 h, 1000–3000 h, and 3000–4000 h), taking into account the visible change in mass with the progress of oxidation. For the reference sample, in the first stage, the k_p value was determined to be 3.18 × 10^{-15}, and in subsequent stages, it decreased to 1.68 × 10^{-15} and 3.04 × 10^{-16}, respectively. In the case of coated samples, the initial values were 4.55 × 10^{-17}, 4.61 × 10^{-17}, and 4.57 × 10^{-17} for CMFO, CMFO-Gd_2O_3, and CMFO-Y_2O_3, respectively. An increase in this parameter was observed for all the samples in the period 1000–3000 h. The determined values of the k_p coefficient for coated steels indicate the beneficial effect of using a thin additional layer. This is especially visible for samples with an additional layer of yttrium oxide.

The values of the k_p coefficient indicate the general corrosion properties of the material. As noticed in this study, k_p values vary with time, so an additional analysis of corrosion kinetics vs. time has been added: the instantaneous parabolic oxidation rate constant. The values of k'_p are independent of their duration and assume a constant value for a process consistent with the parabolic law. The net oxidation rate constant k'_p can be calculated by summing the instantaneous values across the measurement range employed in the experiments, according to the formula [66]:

$$k'_p = \sum_{i=1}^{N} \left(\frac{k_g^i + k_g^{i+1}}{2}\right)\left(\frac{t_{i+1} - t_i}{t_N - t_{i+1}}\right) \quad (2)$$

where k'_p is the instantaneous parabolic oxidation rate constant (g^2 cm^{-4} s^{-1}), t is the oxidation time [s], and N represents the number of measurement points.

When the increase in the scale follows the parabolic oxidation rule

Table 2
Calculated k_p values for corrosion experiments.

k_p coefficient × 10^{-15} g^2 cm^{-4} s^{-1}				
Time interval (h)	Reference	CMFO	CMFO-Gd_2O_3	CMFO-Y_2O_3
0–1000	3.18	0.0455	0.0461	0.0457
1000–3000	1.68	0.105	0.189	0.0907
3000–4000	0.304	0.226	0.361	0.236

across all temperatures, the ratio of k_p to k'_p is close to 1. The determined net oxidation rate constants (k_p') are presented in Table 3. The k'_p/k_p ratio, which is used to determine the departure from parabolic oxidation kinetics, is presented in Table 4. The determined values of the instantaneous parabolic oxidation rate do not differ significantly from the parabolic law for each type of presented samples. This indicates that the use of additional thin layers does not significantly affect the corrosion mechanisms. For samples covered with protective layers at the last stage of oxidation, these values are closest to 1, which is well described by the parabolic rate law.

The determined corrosion coefficients showed compliance of the oxidation process with the parabolic law, and the obtained values for Crofer 22 APU steel should be compared with the available literature data. Previous work for the same steel showed a k_p coefficient of 1.26×10^{-15} in the range of 250–1000 h and 0.47×10^{-15} in the range of 1000–2000 h [18]. Talic et al. determined this parameter for Crofer 22H steel as 3.2×10^{-15} at 750 °C for 2000 h [67]. Koszelow et al. showed a value of 4.5×10^{-15} for porous Fe22Cr steel after an oxidation time of 100 h [68]. Shahbaznejad et al. received a value of 2.54×10^{-13} for Crofer 22 APU steel oxidised for 200 h isothermally at 700 °C [69]. Ignaczak et al. obtained values of this coefficient equal to 3.76×10^{-15} and 2.28×10^{-14} for oxidation times of 0–500 h and 500–3000 h at 750 °C [39]. In the case of Crofer 22H steel coated with MCO, Talic et al. reported that the parabolic oxidation coefficient was 9×10^{-16} after 2000 h at 750 °C [64]. In another work, where the coated material was spinel MCO, $MnCo_{1.7}Fe_{0.3}O_4$, and $MnCo_{1.7}Cu_{0.3}O_4$, the k_p coefficient at 700 °C was 5.5×10^{-16}, 6.9×10^{-16} and 1.1×10^{-15} at 700 °C, respectively, for an oxidation time of 4000 h [29]. Ignaczak et al. reported k_p values for Crofer 22 APU steels coated with MnCuFe0, MnCuFe01, and MnCuFe03 spinel of 6.1×10^{-15}, 4.92×10^{-15}, and 4.73×10^{-15}, respectively, at 750 °C for isothermal oxidation for 3000 h [39]. The obtained values of the k_p coefficient are comparable to those reported in the literature. No significant differences are observed for both uncoated steel and the proposed protective layer.

3.3. Electrical resistivity measurement

The interconnects should have a working life of close to 40,000 h and should not exceed the ASR value of 0.1 Ω cm^2 [70]. Fulfilling these two conditions is necessary to obtain adequate efficiency. The results obtained for cross-scale electrical resistance measurements are shown in Fig. 3A–C. In addition, Supplementary Figs. S4A and S4B show the calculated ASR values after the 1000- and 2000-h stages, and Figs. S4 C and S4 D show the activation energy values calculated based on the measurements divided into two stages: high-temperature (700–550 °C) and low-temperature (500–300 °C).

For samples with an oxidation time of zero hours (i.e., for samples with layers and after the heat treatment process and the bare Crofer steel as reference), the ASR values were 7.62 mΩ cm^2, 14.92 mΩ cm^2, 11.47 mΩ cm^2, and 8.07 mΩ cm^2 for the reference sample, CMFO, CMFO-Gd_2O_3, and CMFO-Y_2O_3 samples, respectively. After the final oxidation stage (4000 h), the ASR values were as follows: 12.89 mΩ cm^2, 14.69 mΩ cm^2, 8.76 mΩ cm^2, 7.37 mΩ cm^2 for the reference sample, CMFO, CMFO-Gd_2O_3 and CMFO-Y_2O_3 samples, respectively. It is also worth noting the changes in the ASR values at lower temperatures. In this case, a significant difference was observed in the slope of the curve for the reference sample at the initial stage and after 4000 h,

Table 3
Determined values of the instantaneous oxidation coefficient.

	k'_p coefficient × 10^{-15} g^2 cm^{-4} s^{-1}			
Time interval (h)	Reference	CMFO	CMFO-Gd_2O_3	CMFO-Y_2O_3
0–1000	13.4	0.182	0.200	0.199
1000–3000	16.8	0.930	1.64	0.843
3000–4000	2.98	1.04	1.69	1.06

Table 4
Determined values of the k'_p/k_p ratio for the coatings used, taking into account the oxidation stages.

	k'_p / k_p			
Time interval (h)	Reference	CMFO	CMFO-Gd_2O_3	CMFO-Y_2O_3
0–1000	4.21	4.11	4.34	4.36
1000–3000	9.99	8.86	8.69	9.30
3000–4000	9.81	4.59	4.69	9.30

and there was no visible difference in the electrical properties of the reference and coated samples. However, the ASR values for samples coated with a protective layer for each of the analysed types indicate a similar character, and the ASR values at 300 °C were between 1 and 2 Ω cm^2. Together with the ongoing oxidation process, we also observe the convergence of ASR values for individual types. These values also match the trend observed in weight gain measurements. After 1000 h of oxidation, we observe that the lowest ASR value can be observed for samples with an additional layer of Gd_2O_3. Also, the lowest weight gain value was observed for the CMFO-Gd_2O_3 samples. In the next oxidation stage, it was observed that the lowest ASR values were measured for the CMFO-Y_2O_3 samples. This result is equivalent to the lowest weight gain. The sample with an additional layer of gadolinium oxide, despite the worst weight gain among the protective layers used, showed a lower ASR value than the sample with spinel only. Mazur et al. determined the ASR values for the $Mn_{1.5}Co_{1.5}O_4$ and $Mn_{1.45}Co_{1.45}Cu_{0.1}O_4$ layers as 21.4 mΩ cm^2 and 29.3 mΩ cm^2 at 750 °C after oxidation for 1200 h at the same temperature[71]. In another work describing the effect of coating Crofer 22 APU steel with double layers of gadolinium oxide and $MnCo_2O_4$ spinel at 800 °C for 7000 h, an ASR of 19 mΩ cm^2 was obtained [45]. Ignaczak et al. determined the ASR values for the same steel coated with MnCuFe0, MnCuFe01, and MnCuFe03 spinel and oxidised at 750 °C for 3000 h as values between 3 and 5 mΩ cm^2 at 750 °C, which were lower values than for samples with an MCO layer and peroxided samples [39]. Sun et al. reported the coating of Crofer 22 APU steel with $Cu_{1.3}Mn_{1.7}O_4$ spinel and oxidation at 800 °C for 185 h. The ASR value obtained for these combinations was 6.13 mΩ cm^2 at 800 °C [34]. Huang et al. indicated an ASR value of 4.6 mΩ cm^2 for the applied layer of coating the same steel with $CuMn_{1.8}O_4$ spinel and oxidisation for 100 h at 800 °C [72].

The activation energy was determined using the slope obtained during the ASR measurements and according to the Arrhenius law:

$$\boldsymbol{ASR = A \bullet \exp\left(\frac{E_a}{kT}\right)} \quad (3)$$

where: A is a pre-exponential factor (Ω cm^{-2} K^{-1}), Ea is the activation energy (kJ mol^{-1}), k is Boltzmann's constant (J K^{-1}) and T is the temperature (K). The initial activation energies were 11.41 kJ mol^{-1}, 36.53 kJ mol^{-1}, 55.06 kJ mol^{-1}, and 44.58 kJ mol^{-1}, for the reference sample, with a $CuMn_{1.7}Fe_{0.3}O_4$ layer, $CuMn_{1.7}Fe_{0.3}O_4$ with Gd_2O_3 layer, and $CuMn_{1.7}Fe_{0.3}O_4$ with Y_2O_3, respectively (in the range 700–550 °C). A very low value is noticeable for the reference sample, which is not surprising since the initial stage of corrosion of uncoated steel is very fast. The highest value of the activation energy was observed for the $CuMn_{1.7}Fe_{0.3}O_4$-Gd_2O_3 samples. After the final stage of oxidation, the value of Ea was 42.98 kJ mol^{-1}, 54.88 kJ mol^{-1}, 39.48 kJ mol^{-1} and 49.96 kJ mol^{-1} for the reference sample, with a $CuMn_{1.7}Fe_{0.3}O_4$ layer, $CuMn_{1.7}Fe_{0.3}O_4$ with Gd_2O_3 layer, and $CuMn_{1.7}Fe_{0.3}O_4$-Y_2O_3, respectively. These values refer to the analysed range in the higher temperature region. Talic et al. obtained activation energy values for $MnCo_{1.7}Fe_{0.3}O_4$ and $MnCo_{1.7}Cu_{0.3}O_4$ protective coatings in the range of 77–78 kJ mol^{-1} for samples aged at 800 °C for 4370 h and 65 kJ mol^{-1} for clean Crofer 22 APU steel [29]. Bednarz et al. determined the activation energies for $Mn_{1.5}Co_{1.5}O_4$ and $Mn_{1.45}Co_{1.45}Fe_{0.1}O_4$ materials oxidised at 800 °C for 1200 h as 52.40 kJ mol^{-1} and 48.44 kJ mol^{-1}, respectively [73]. The obtained data are comparable with the literature

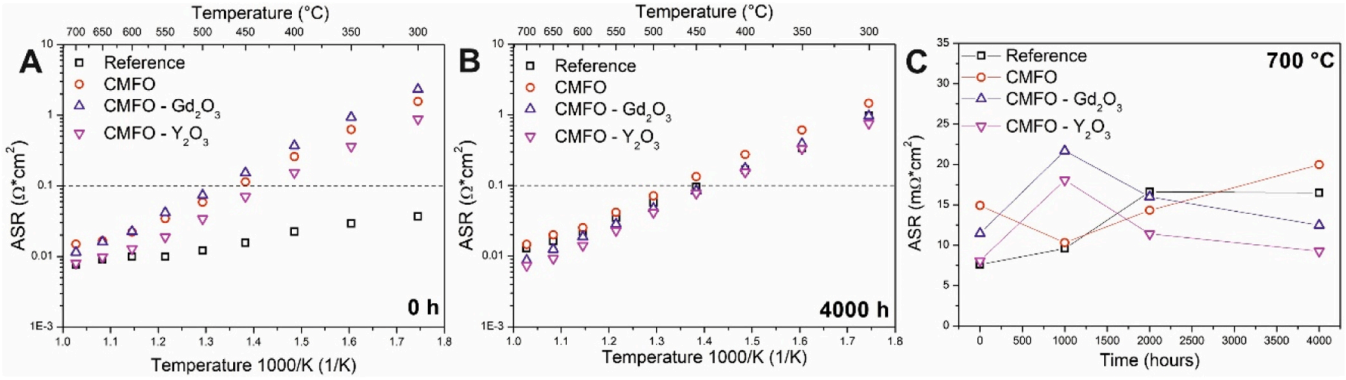

Fig. 3. Arrhenius plots of the surface resistance of samples oxidised at 700 °C for 0 h (A) and 4000 h (B) and comparison of the ASR value at 700 °C over time.

data. Comparisons are mainly at higher temperatures, as corrosion analysis at low temperatures (700 °C) is still largely unknown. However, these values are rational and do not differ from the literature trend.

3.4. XRD and SEM analysis

XRD measurements and SEM analysis of post-mortem samples were also performed. Fig. S5 shows the XRD measurement after 4000 h stages to check the stability of the material over time. The obtained diffraction spectrum makes it possible to identify the main phase in the form of a cubic structure (space group: *Fd*-3*m*) of the $CuMn_{1.7}Fe_{0.3}O_4$ spinel. For samples where the only protective layer is CMFO, small peaks at 29° and 57° were also identified, indicating the presence of MnO_2 in the coating. However, there are no observations of peaks corresponding to Cr_2O_3 and $MnCr_2O_4$ formed during oxidation. For layers with an additional RE oxide protective layer in the case of CMFO-Gd_2O_3, an additional peak is observed at 32.5°, which identified the tetragonal phase (space group: *I*41/*amd:2*). As in the case of CMFO, no peaks corresponding to Cr_2O_3/$MnCr_2O_4$ corrosion were observed and there was no signal from RE oxide in the form of Y_2O_3 or Gd_2O_3. There were also no peaks responsible for $YMnO_3$ or $GdCrO_3$ formed during the oxidation, the existence of which was confirmed in previous work [18].

Fig. 4 presents cross-section images for the sample with the $CuMn_{1.7}Fe_{0.3}O_4$ spinel (Fig. 4A), for the sample with an additional layer of gadolinium oxide (4B), and for the sample with an additional layer of yttrium oxide (4 C) obtained for samples subjected to corrosion for 4000 h at 700 °C. The darker layer visible near the surface of the steel indicates that a very thin layer of Cr_2O_3/$MnCr_2O_4$ had formed. SEM images show a thin layer of chromium oxide (thickest for the sample with CMFO layer). A layer of dense spinel is also observed close to the steel surface. A thin gadolinium oxide-based layer was observed on the Gd_2O_3-modified sample. On the Y_2O_3-modified sample, a discontinuous Y_2O_3 thin layer was observed. Despite these microstructural differences, as shown in Section 3.2, it revealed good corrosion protection properties. Fig. S6 show SEM images showing a larger area of the analysed samples.

Fig. S7 depicts an SEM-EDS analysis illustrating the elemental distribution within the layer. It was demonstrated that there exists a chromium-rich layer in direct contact with the steel. Moreover, noticeable in samples with a CMFO layer are regions of heightened intensity closer to the layer's surface, indicating chromium diffusion through the layer. In samples CMFO-Gd_2O_3 and CMFO-Y_2O_3, a distinct border of chromium oxide occurrence is observed, coinciding with the presence of an additional layer. The discontinuous nature of the Y_2O_3 layer was observed in previous work [18]. Line scans were conducted on the discussed sample types to further understand and illustrate the blocking of chromium diffusion. The obtained line scans are shown in Fig. S8. For the CMFO sample, after 4000 h, a region corresponding to the chromium oxide layer is visible at the peak chromium concentration. The chromium content gradually decreases until reaching the surface area. In samples with an additional layer of gadolinium oxide or yttrium oxide, a distinct flattening of the chromium line after the layer is observed, indicating blocking of chromium diffusion. The inherent blocking capacity of the CMFO layer alone is limited, as demonstrated in prior studies on similar materials. The inclusion of a thin additional layer of yttrium or gadolinium oxide results in a slight reduction in chromium diffusion, possibly influenced by the discontinuous nature and small thickness (~ 100 nm) of the yttrium oxide layer. Reddy et al. described the coating of Crofer 22 APU steel with various protective materials, including $CuMn_{1.8}O_4$ compared to MCO, and compared, among others, chromium evaporation. EDS analysis after 3000 h of oxidation at 800 °C showed that the layer composed of $CuMn_{1.8}O_4$ had the worst parameters

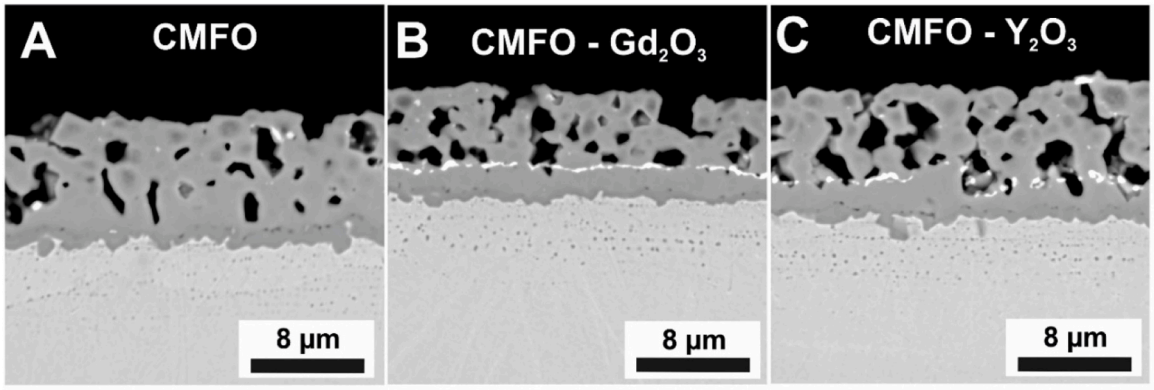

Fig. 4. SEM pictures taken for samples after oxidation for 4000 h at 700 °C. Cross-sections obtained for a sample with a layer of spinel $CuMn_{1.7}Fe_{0.3}O_4$ (A), spinel and gadolinium oxide (B), and spinel and yttrium oxide (C).

for blocking chromium diffusion. In this case, a gradual decrease in the amount of chromium is visible. In the case of MCO, much smaller diffusion is observed, and the chromium map indicates a very small content of chromium diffused into the layer itself [74]. The reason for this may be the greater solubility of chromium in the Cu and Mn-based spinel layers. It has been shown that $CuMn_2O_4$ spinel is an excellent getter of chromium (or chromium oxide) [75]. A similar relationship in EDS maps, like for $CuMn_{1.8}O_4$, is observed for the CMFO layer. A clear change in the slope of the curve in line scans observed for samples with an additional layer indicates an increase in the degree of chromium blocking, but not completely preventing it. Spot measurements were also conducted to precisely determine the chromium content in individual layer parts. The data presented in Fig. S9B were gathered from four points distributed along the layer (Fig. S9A). Chromium content is comparable across all samples at the point nearest to the steel surface. However, a notable reduction in chromium content is observed at the second point for CMFO-Gd_2O_3 and CMFO-Y_2O_3 samples. Chromium concentrations for points closer to the surface have the lowest chromium concentration and comparable across all types. It is also worth noting that the chromium content near the surface is low and a large error is possible at this point with EDS spot analysis. In the case of the comparison of the coefficient between the atomic content of manganese and copper (presented in Fig. S8C), it was shown that the area rich in chromium oxide and the reactive layer have a significantly different coefficient from the basic one. This indicates the potential decomposition of spinel by chromium diffusing into the layer. For the two analysed points further away from the steel surface, it is visible that this coefficient has values close to the target value. This also indicates the lack of degradation of the material itself and the decomposition of spinel into various oxides.

The SEM-EDS analyses presented in the form of element identification mapping, line scans, and point analysis of the layer demonstrated an enhancement in blocking chromium diffusion compared to samples with only a CMFO spinel layer. This enhancement is associated with the presence of a thin layer of Gd_2O_3 or Y_2O_3. However, the extent of improvement is constrained by the low thickness of the additional layer and its discontinuous nature.

3.5. Confocal Raman imaging

In order to describe and understand the reactions between Crofer 22 APU steel, protective layers, and oxygen, measurements were made using Raman Confocal Imaging. For this purpose, samples that had undergone 4000 h of oxidation were selected from among the CMFO, CMFO-Gd_2O_3, and CMFO-Y_2O_3 specimens and were cross-sectioned and polished. Similarly to literature reports [45,76], the formation of two very typical phases for Crofer 22APU below the protective coating was confirmed with Raman Confocal imaging (Fig. 5) – Cr_2O_3 based on bands at ca. 296, 352, 555 (the most characteristic ones) and 616 cm^{-1} [77], as well as $(Mn,Cr)_3O_4$ spinel based on Raman modes at around 509 and 691 cm^{-1} [78]. Moreover, bands at ca. 430 and 541 cm^{-1} were observed for the thickest, top layer, which is composed of CuMnFe spinel [79,80]. As can be seen, two spectra of a very similar shape, especially within the 350–700 cm^{-1} spectral range, were determined – the only, but easily noticeable difference concerns the opposite intensity relation of characteristic bands coming from CuMnFe spinel (541 cm^{-1}) and MnO_2 (622 cm^{-1} [81]) located mainly in the upper part of the protective coating. For specimens with additional protection in the form of Y_2O_3 (Fig. 4B) and Gd_2O_3 (Fig. 4C), results similar to first sample, which were also alike, were obtained – in both cases, Cr_2O_3, Mn-Cr spinel and protective $CuMn_{1.7}Fe_{0.3}O_4$ spinel mixed with MnO_2 were found. In this case, it was impossible to differentiate the location of protective spinel and MnO_2, which suggests the scattering of the latter within the whole coating. As far as Y- and Gd-based phases are concerned, two intriguing observations were made. Firstly, no bands typical for Y_2O_3 and Gd_2O_3 were noticed. Secondly, different type of perovskite-like non-continuous phases were formed, just above the Mn-Cr spinel, depending on the applied oxide – for yttria, $YMnO_3$ was formed (bands at ca. 224, 418, 448, 637, and 691 cm^{-1} [82]) and for gadolinium, it is probable that $GdCrO_3$ or $GdMn_{1-x}Cr_xO_3$ (with x close to 1) was nucleated (modes at around 222, 330, 634, 690 cm^{-1} [83]). Mazur et al. described the formation of a similar Gd-based perovskite--like structure, but for a different protective spinel ($MnCo_2O_4$) [45]. In a previous study that only focused on protective ceramic layers, similar results were also noticed. In that study, the formation of perovskite compounds based on Y and Gd, as well as phases of chromium oxide and manganese-chromium spinel, standard for Crofer 22 APU steel, was observed [18]. The identification of the $YMnO_3$ layer as the reaction product of yttrium during oxidation is an interesting observation. Linescans performed for CMFO-Gd_2O_3 and CMFO-Y_2O_3 samples indicate an increased concentration of manganese near the RE-oxide layer. This may also indicate the reason for the occurrence of $YMnO_3$. In the literature, most often, $YCrO_3$ is identified as a result of the reaction of yttrium oxide and chromium oxide formed during oxidation [18,84,85]. The only work found in which $YMnO_3$ was present described the coating of AISI 430 steel with a layer of Y_2O_3. However, in the cited work, the XRD peaks identified as $YMnO_3$ were small, and the remaining peaks obscured them [86,87]. The influence of the transformation of yttrium oxide and gadolinium oxide on perovskite compounds is also visible in those described in Section 3.3 by observing lower ASR values for the CMFO-Y_2O_3 and CMFO-Gd_2O_3 samples, even despite the greater weight gain for the second type. The reason for this is that perovskite oxides are characterised by much higher electronic conductivity than reactive element oxides. Additionally, the highest ASR value was observed for the sample with only spinel, which is probably related to the significant amount of manganese oxide observed in this study.

3.6. XAS spectroscopy

To supplement the discussion on the characteristics of the $CuMn_{1.7}Fe_{0.3}O_4$ spinel material and the impact of interactions with other materials, such as the applied ceramic layers and the Crofer 22 APU steel itself, a series of X-ray absorption spectroscopy (XAS) measurements was taken. The obtained Cu L_3-edge spectra for copper are presented in Fig. 6A. Analogous measurements for manganese and iron electronic surrounding are shown in Fig. 6B and Fig. 6C, respectively. The absorption edges of the Cu reference powders were observed at 938.85 eV for CuO and 931.55 eV for Cu_2O. This is in line with the standardised data recorded previously for Cu oxides. In case of the copper-manganese-iron spinel analysis, a sharp band at ~ 938.85 eV was observed in all cases, which indicates the presence of copper in the Cu^{2+} oxidation state. The observed peaks indicate the excitation of the Cu 2p electron, which under the influence of the energy quantum, goes to a higher energy level, in this case 3d, occupying the unoccupied band and resulting in the $2p^5$ $3d^{10}$ configuration [87]. The obtained spectra correspond to the presence of copper as a divalent cation within the A-site in the spinel structure [88]. A more complex situation is observed in the case of manganese. For the MnO, the absorption edge white line was observed at 640.2 eV, for the Mn_2O_3 at 642.2 eV, and for the MnO_2 at 642.9 eV, respectively. For manganese in the Mn^{2+} oxidation state, the observed binding energy value of the edge can stand for high-spin manganese ions in the $3d^5$ configuration. Respectively, for the Mn^{3+} oxidation state, the electronic configuration of $3d^4$ was recorded, and the $3d^3$ configuration for the Mn^{4+} ions [89]. The manganese ions in the $CuMn_{1.7}Fe_{0.3}O_4$ spinel were found to be in mixed valence, occupying all three oxidation states. A change in the valence after the exposure to an oxidising environment was also observed. With the CMFO and CMFO-Gd_2O_3 samples, a decrease in the oxidation state of the Mn oxidation state was observed in relation to the initial data, while the Mn^{3+} and Mn^{2+} bands became more pronounced at 640.2 eV and 642.2 eV, respectively. In contrast, for the samples with an additional layer of yttrium oxide, the transition of manganese to higher oxidation

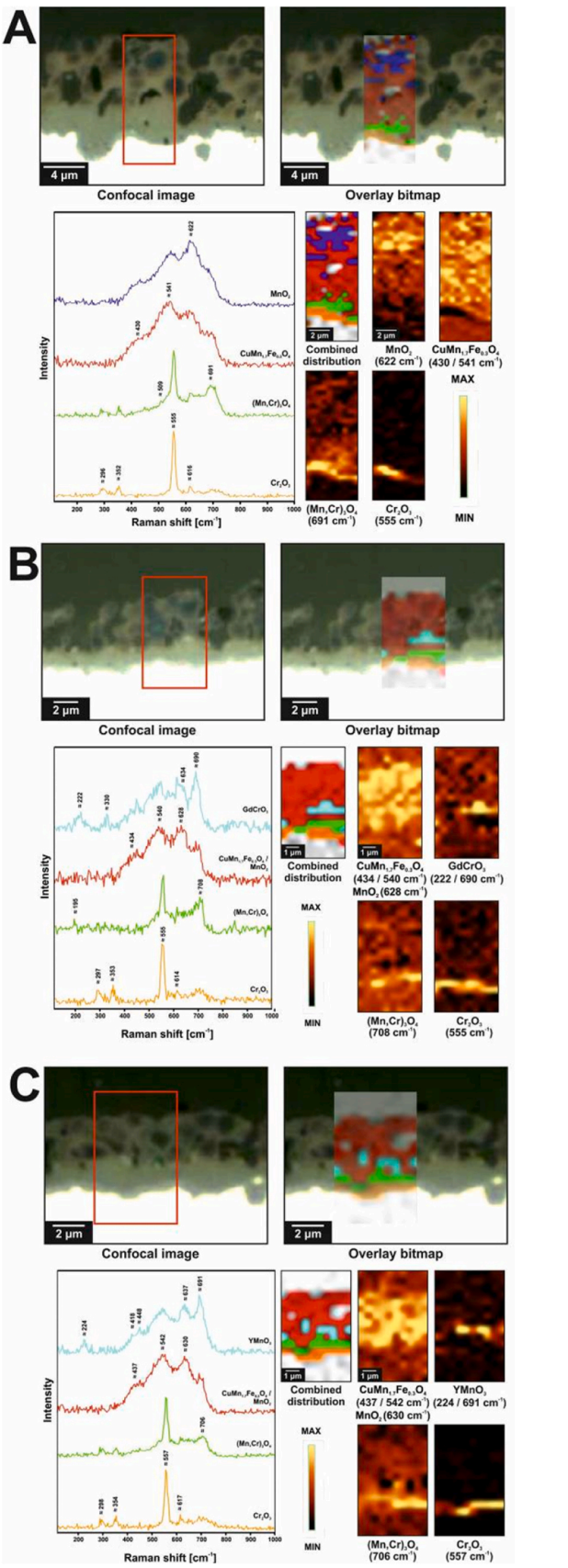

(caption on next column)

Fig. 5. Raman Confocal imaging for Crofer 22 APU steel samples with a protective layer of $CuMn_{1.7}Fe_{0.3}O_4$ (A), $CuMn_{1.7}Fe_{0.3}O_4$-Gd_2O_3 (B) and $CuMn_{1.7}Fe_{0.3}O_4$-Y_2O_3(C) after 4000 h of oxidation at 700 °C. For all Raman data: red square in confocal image corresponds to area investigated with Raman laser. Raman distribution images (obtained via the integration of the most characteristic band for the specific phase along with value of its Raman shift given in the brackets) are illustrated with the Raman spectra. Each spectrum was also marked with bands that can be unequivocally attributed to corresponding phase(s).

states was observed. For the Fe reference powder, the absorption edges were observed at 708.3 eV (corresponding to Fe^{2+}) and at 709.7 eV (the characteristic maximum for Fe^{3+}). The Fe L_3-edge of the spinel-only-covered sample was located at 709.7 eV, which implies that most of the iron ions had undergone Fe^{3+} oxidation. This indicates a successful occupancy of the octahedral position of the $3d^5$ trivalent iron in the spinel B-site structure [89]. No significant differences after the corrosion tests were observed for both copper and iron. Copper occupies the spinel's tetrahedral A-site, and trivalent iron resides in the B-site of the spinel. Only minor changes were observed for the manganese valence. XAS measurements indicate differences that occur in the material during oxidation (specifically in the case of Mn). For the CMFO samples, the MnO_2 that was seen in the CRI and XRD measurements could not be found in the XAS, probably due to the possibility because only the sample's surface could be analysed.

4. Conclusions

This work demonstrated the potential of using $CuMn_{1.7}Fe_{0.3}O_4$ spinel with thin additional protective layers (Gd_2O_3, Y_2O_3) to protect interconnectors at 700 °C. The material was characterised using TPR, which showed that reduction begins at approximately 250 °C with Cu reducing to metallic copper. The spinel exhibited a lower reduction temperature compared to MCO, influenced by the presence of metallic Cu.

Electrophoretic deposition technique allowed for adequate application of protective layers on Crofer 22 APU steel. Three coating types were tested: spinel only (CMFO), spinel with gadolinium oxide (CMFO-Gd_2O_3), and spinel with yttrium oxide (CMFO-Y_2O_3). These were oxidised at 700 °C for 4000 h. The CMFO-Y_2O_3 coating demonstrated the lowest weight gain, while the other samples showed slightly higher values. Electrical resistivity measurements revealed low Area Specific Resistance (ASR) values for all coated samples, with no significant increase in ASR or activation energy observed throughout the analysis period.

Comprehensive material analysis after oxidation was conducted using SEM-EDS, Confocal Raman imaging (CRI), X-ray Absorption Spectroscopy (XAS), and X-ray Diffraction (XRD). These techniques indicated the presence of standard phases in Crofer 22 APU steel, including chromium oxide and manganese-chromium spinel. The additional yttria and gadolinium oxide coatings resulted in the formation of $YMnO_3$ and $GdCrO_3$ perovskite phases, respectively. These analyses also confirmed the presence of a low content of the MnO_2 phase.

Spot and linescan microscopic analyses confirmed enhanced chromium diffusion blocking in samples with additional RE-oxide layers. This is particularly significant due to the nature of copper manganese spinels, which typically show weaker chromium diffusion blocking compared to state-of-the-art $(Mn,Co)_3O_4$.

XAS measurements carried out on samples with different oxidation times detected changes occurring in the structure of the protective layer after subsequent stages of oxidation. No changes in the oxidation state of copper and iron were observed. During the oxidation process, the significant changes were observed with the manganese, where shifts towards a higher oxidation state (CMFO-Y_2O_3) or towards a lower one (for other types of samples) were observed. A graphical summary of the impact of the additional reactive element layer is presented in the Fig. 7.

The proposed new combination of coating represents a viable

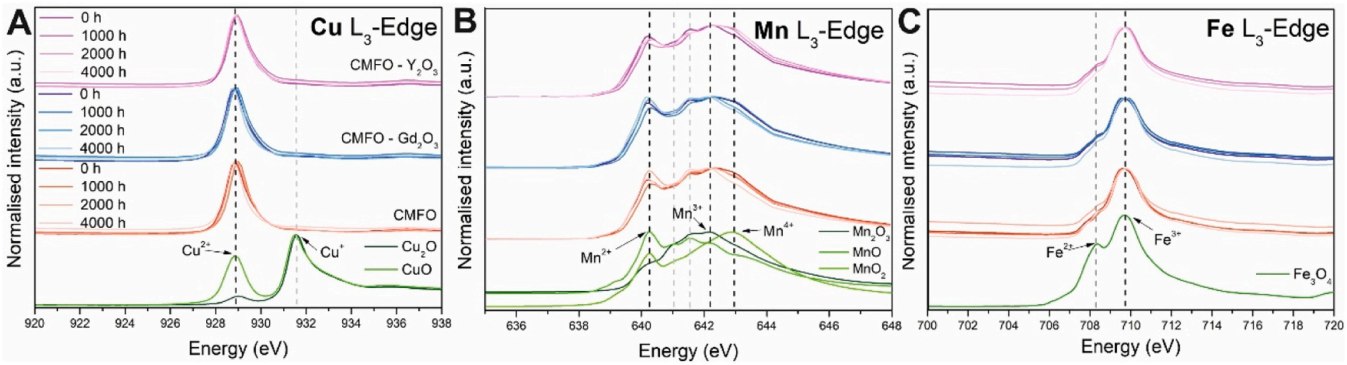

Fig. 6. XAS spectra collected for samples after different oxidation times for the L3 edge of copper (A), manganese (B), and iron (C).

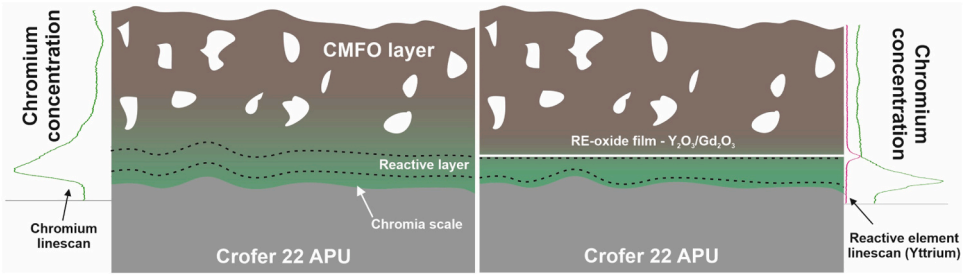

Fig. 7. Sketch explaining the effect of an additional layer in blocking chromium diffusion.

alternative to the state-of-the-art $(Mn,Co)_3O_4$ spinels. The tested materials are free of cobalt, while maintaining its protective and even improving the electrical properties. The effective reduction of cobalt in SOC materials opens the door to an effective reduction in production costs and dispels doubts in the context of possible health and environmental issues.

CRediT authorship contribution statement

Maciej Bik: Writing – review & editing, Writing – original draft, Methodology, Investigation. **Piotr Jasiński:** Writing – review & editing, Supervision, Methodology, Funding acquisition, Conceptualization. **Sebastian Molin:** Writing – review & editing, Writing – original draft, Supervision, Methodology, Conceptualization. **Marcin Zając:** Writing – review & editing, Methodology, Investigation. **Maciej Sitarz:** Writing – review & editing, Methodology. **Bartłomiej Lemieszek:** Writing – review & editing, Writing – original draft, Methodology, Investigation. **Justyna Ignaczak:** Writing – review & editing, Methodology, Investigation. **Krystian Lankauf:** Writing – review & editing, Methodology, Investigation. **Patryk Błaszczak:** Writing – review & editing, Methodology, Investigation.

Declaration of Competing Interest

The authors declare the following financial interests/personal relationships which may be considered as potential competing interests: Piotr Jasinski reports financial support was provided by National Science Centre Poland. If there are other authors, they declare that they have no known competing financial interests or personal relationships that could have appeared to influence the work reported in this paper.

Data availability

The raw/processed data required to reproduce these findings cannot be shared at this time as the data also forms part of an ongoing study.

Acknowledgement

This research has been supported by National Science Centre (NCN) Harmonia 9 Project no. UMO-2017/26/M/ST8/00438: 'Quest for novel materials for solid oxide cell interconnect coatings'. This publication was partially developed under the provision of the Polish Ministry and Higher Education project 'Support for research and development with the use of research infra-structure of the National Synchrotron Radiation Centre SOLARIS' under Contract nr. 1/SOL/2021/2. The authors would like to acknowledge MSc Patryk Zając from AGH UST for his help during the execution of the Raman Confocal Imaging.

Declaration of Competing Interest

The authors declare that they have no known competing financial interests or personal relationships that could have appeared to influence the work reported in this paper.

Appendix A. Supporting information

Supplementary data associated with this article can be found in the online version at doi:10.1016/j.jeurceramsoc.2024.116743.

References

[1] N. Shaigan, W. Qu, D.G. Ivey, W. Chen, A review of recent progress in coatings, surface modifications and alloy developments for solid oxide fuel cell ferritic stainless steel interconnects, J. Power Sources 195 (2010) 1529–1542, https://doi.org/10.1016/J.JPOWSOUR.2009.09.069.
[2] N. Mahato, A. Banerjee, A. Gupta, S. Omar, K. Balani, Progress in material selection for solid oxide fuel cell technology: a review, Prog. Mater. Sci. 72 (2015) 141–337, https://doi.org/10.1016/j.pmatsci.2015.01.001.
[3] S. Chevalier, L. Combemale, I. Popa, S. Chandra-Ambhorn, W. Chandra-Ambhorn, P. Promdirek, P. Wongpromrat, Development of sofc interconnect stainless steels, Solid State Phenom. 300 (2020) 135–156, https://doi.org/10.4028/www.scientific.net/SSP.300.135.
[4] Z. Yang, J.E. Soc, Z. Yang, K.S. Weil, D.M. Paxton, J.W. Stevenson, Selection and Evaluation of Heat-Resistant Alloys for SOFC Interconnect Applications Selection and Evaluation of Heat-Resistant Alloys for SOFC Interconnect Applications, 2003. ⟨https://doi.org/10.1149/1.1595659⟩.

[5] S. Canovic, J. Froitzheim, R. Sachitanand, M. Nikumaa, M. Halvarsson, L. G. Johansson, J.E. Svensson, Oxidation of Co- and Ce-nanocoated FeCr steels: a microstructural investigation, Surf. Coat. Technol. 215 (2013) 62–74, https://doi.org/10.1016/J.SURFCOAT.2012.08.096.

[6] A. Magrasó, H. Falk-Windisch, J. Froitzheim, J.E. Svensson, R. Haugsrud, Reduced long term electrical resistance in Ce/Co-coated ferritic stainless steel for solid oxide fuel cell metallic interconnects, Int. J. Hydrog. Energy 40 (2015) 8579–8585, https://doi.org/10.1016/J.IJHYDENE.2015.04.147.

[7] F. Saeidpour, M. Zandrahimi, H. Ebrahimifar, Evaluation of pulse electroplated cobalt/yttrium oxide composite coating on the Crofer 22 APU stainless steel interconnect, Int. J. Hydrog. Energy 44 (2019) 3157–3169, https://doi.org/10.1016/J.IJHYDENE.2018.12.062.

[8] X. Deng, P. Wei, M.R. Bateni, A. Petric, Cobalt plating of high temperature stainless steel interconnects, J. Power Sources 160 (2006) 1225–1229, https://doi.org/10.1016/J.JPOWSOUR.2006.03.024.

[9] K. Huang, P.Y. Hou, J.B. Goodenough, Reduced area specific resistance for iron-based metallic interconnects by surface oxide coatings, Mater. Res. Bull. 36 (2001) 81–95, https://doi.org/10.1016/S0025-5408(01)00506-2.

[10] S. Molin, H. Persson, T.L. Skafte, A.L. Smitshuysen, S.H. Jensen, K.B. Andersen, H. Xu, M. Chen, P.V. Hendriksen, Effective yttrium based coating for steel interconnects of solid oxide cells: corrosion evaluation in steam-hydrogen atmosphere, J. Power Sources 440 (2019), https://doi.org/10.1016/j.jpowsour.2019.226814.

[11] L. Yang, X. Pang, G. Fox-Rabinovich, S. Veldhuis, I. Zhitomirsky, Electrodeposition of cerium oxide films and composites, Surf. Coat. Technol. 206 (2011) 1–7, https://doi.org/10.1016/j.surfcoat.2011.06.029.

[12] I. Zhitomirsky, A. Petric, Electrolytic and electrophoretic deposition of CeO2 films, Mater. Lett. 40 (1999) 263–268, https://doi.org/10.1016/S0167-577X(99)00087-7.

[13] I. Zhitomirsky, A. Petric, Electrochemical deposition of yttrium oxide, J. Mater. Chem. 10 (2000) 1215–1218, https://doi.org/10.1039/b000311p.

[14] J.S. Yoon, J. Lee, H.J. Hwang, C.M. Whang, J.W. Moon, D.H. Kim, Lanthanum oxide-coated stainless steel for bipolar plates in solid oxide fuel cells (SOFCs), J. Power Sources 181 (2008) 281–286, https://doi.org/10.1016/J.JPOWSOUR.2007.12.053.

[15] Ł. Mazur, J. Pleśniak, J. Dąbek, A. Gil, T. Brylewski, High-temperature oxidation of ferritic steel surface-modified with gadolinium oxide nanoparticles, Ceram. Mater. 71 (2019) 179–192.

[16] L. Venkataraman, R. Ae, M.F. Pillis, A.E. Stela, M.C. Fernandes, Role of rare earth oxide coatings on oxidation resistance of chromia-forming alloys, J. Mater. Sci. 43 (2008) 530–535, https://doi.org/10.1007/s10853-007-1855-8.

[17] A. Balland, P. Gannon, M. Deibert, S. Chevalier, G. Caboche, S. Fontana, Investigation of La_2O_3 and/or $(Co,Mn)_3O_4$ deposits on Crofer22APU for the SOFC interconnect application, Surf. Coat. Technol. 203 (2009) 3291–3296, https://doi.org/10.1016/J.SURFCOAT.2009.04.017.

[18] B. Lemieszek, J. Ignaczak, B. Kamecki, J. Karczewski, M.B. Mogensen, S. Molin, P. Jasiński, Electrolytic deposition of reactive element thin films on Crofer 22 APU and evaluation of the resulting high-temperature corrosion protection properties at 700–900 °C, Int. J. Hydrog. Energy 47 (2022) 33453–33465, https://doi.org/10.1016/J.IJHYDENE.2022.07.220.

[19] N. Orlovskaya, A. Coratolo, C. Johnson, R. Gemmen, Structural characterization of lanthanum chromite perovskite coating deposited by magnetron sputtering on an iron-based chromium-containing alloy as a promising interconnect material for SOFCs, J. Am. Ceram. Soc. 87 (2005), https://doi.org/10.1111/j.1151-2916.2004.tb06350.x.

[20] N. Shaigan, D.G. Ivey, W. Chen, Oxidation and electrical behavior of nickel/lanthanum chromite-coated stainless steel interconnects, J. Power Sources 183 (2008) 651–659, https://doi.org/10.1016/j.jpowsour.2008.05.024.

[21] X. Montero, N. Jordán, J. Pirón-Abellán, F. Tietz, D. Stöver, M. Cassir, I. Villarreal, Spinel and perovskite protection layers between Crofer22APU and $La_{0.8}Sr_{0.2}FeO_3$ cathode materials for SOFC interconnects, J. Electrochem. Soc. 156 (2009) B188, https://doi.org/10.1149/1.3025914.

[22] Z. Yang, G.-G. Xia, G.D. Maupin, J.W. Stevenson, Evaluation of perovskite overlay coatings on ferritic stainless steels for SOFC interconnect applications, J. Electrochem. Soc. 153 (2006) A1852, https://doi.org/10.1149/1.2239371.

[23] N.S. Waluyo, R.-H. Song, S.-B. Lee, T.-H. Lim, S.-J. Park, J.-W. Lee, Electrophoretically deposited $LaNi_{0.6}Fe_{0.4}O_3$ perovskite coatings on metallic interconnects for solid oxide fuel cells, J. Electrochem. Soc. 163 (2016) F1245–F1250, https://doi.org/10.1149/2.1171610jes.

[24] R. Lacey, A. Pramanick, J.C. Lee, J.Il Jung, B. Jiang, D.D. Edwards, R. Naum, S. T. Misture, Evaluation of Co and perovskite Cr-blocking thin films on SOFC interconnects, Solid State Ion. 181 (2010) 1294–1302, https://doi.org/10.1016/J.SSI.2010.07.007.

[25] B.-K. Park, R.-H. Song, S.-B. Lee, T.-H. Lim, S.-J. Park, C.-O. Park, J.-W. Lee, A perovskite-type lanthanum cobaltite thin film synthesized via an electrochemical route and its application in SOFC interconnects, J. Electrochem. Soc. 162 (2015) F1549–F1554, https://doi.org/10.1149/2.0901514jes.

[26] A. Masi, S. Frangini, D. Pumiglia, L. Della Seta, A. Masci, S.J. Mcphail, M. Carlini, $LaFeO_3$ perovskite conversion coatings grown on a 13Cr ferritic stainless steel: a corrosion degradation study in simulated solid oxide fuel cell (SOFC) interconnect conditions, at 700 (2016) 8C.

[27] R.J. Hill, J.R. Craig, G.V. Gibbs, PHYSICS I] CHEMISTRY MIHERALS Systematics of the Spinel Structure Type, 1979.

[28] J. Xiao, W. Zhang, C. Xiong, B. Chi, J. Pu, L. Jian, Oxidation of $MnCu_{0.5}Co_{1.5}O_4$ spinel coated SUS430 alloy interconnect in anode and cathode atmospheres for intermediate temperature solid oxide fuel cell, Int. J. Hydrog. Energy 40 (2015) 1868–1876, https://doi.org/10.1016/J.IJHYDENE.2014.11.124.

[29] B. Talic, S. Molin, K. Wiik, P.V. Hendriksen, H.L. Lein, Comparison of iron and copper doped manganese cobalt spinel oxides as protective coatings for solid oxide fuel cell interconnects, J. Power Sources 372 (2017) 145–156, https://doi.org/10.1016/J.JPOWSOUR.2017.10.060.

[30] D. Szymczewska, S. Molin, P. Vang Hendriksen, P. Jasí Nski, Microstructure and Electrical Properties of Fe,Cu Substituted $(Co,Mn)_3O_4$, Thin, Films (2017).

[31] A. Masi, M. Bellusci, S.J. McPhail, F. Padella, P. Reale, J.E. Hong, R. Steinberger-Wilckens, M. Carlini, The effect of chemical composition on high temperature behaviour of Fe and Cu doped Mn-Co spinels, Ceram. Int. 43 (2017) 2829–2835, https://doi.org/10.1016/J.CERAMINT.2016.11.135.

[32] S. Joshi, A. Petric, Nickel substituted $CuMn_2O_4$ spinel coatings for solid oxide fuel cell interconnects, Int. J. Hydrog. Energy 42 (2017) 5584–5589, https://doi.org/10.1016/J.IJHYDENE.2016.08.075.

[33] Z. Sun, R. Wang, A.Y. Nikiforov, S. Gopalan, U.B. Pal, S.N. Basu, $CuMn_{1.8}O_4$ protective coatings on metallic interconnects for prevention of Cr-poisoning in solid oxide fuel cells, J. Power Sources 378 (2018) 125–133, https://doi.org/10.1016/J.JPOWSOUR.2017.12.031.

[34] Z. Sun, S. Gopalan, U.B. Pal, S.N. Basu, $Cu_{1.3}Mn_{1.7}O_4$ spinel coatings deposited by electrophoretic deposition on Crofer 22 APU substrates for solid oxide fuel cell applications, Surf. Coat. Technol. 323 (2017) 49–57, https://doi.org/10.1016/J.SURFCOAT.2016.09.028.

[35] S.R. Akanda, N.J. Kidner, M.E. Walter, Spinel coatings on metallic interconnects: effect of reduction heat treatment on performance, Surf. Coat. Technol. 253 (2014) 255–260, https://doi.org/10.1016/J.SURFCOAT.2014.05.049.

[36] B.K. Sovacool, The precarious political economy of cobalt: balancing prosperity, poverty, and brutality in artisanal and industrial mining in the Democratic Republic of the Congo, Extr. Ind. Soc. 6 (2019) 915–939, https://doi.org/10.1016/J.EXIS.2019.05.018.

[37] D. Lison, S. Van Den Brule, G. Van Maele-Fabry, Critical Reviews in Toxicology Cobalt and its compounds: update on genotoxic and carcinogenic activities Cobalt and its compounds: update on genotoxic and carcinogenic activities, 2018. ⟨https://doi.org/10.1080/10408444.2018.1491023⟩.

[38] J. Ignaczak, Y. Naumovich, K. Górnicka, J. Jamroz, W. Wróbel, J. Karczewski, M. Chen, P. Jasi, S. Molin, Preparation and characterisation of iron substituted $Mn_{1.7}Cu_{1.3-x}Fe_xO_4$ spinel oxides (x = 0, 0.1, 0.3, 0.5), J. Eur. Ceram. Soc. (2020) 1–10, https://doi.org/10.1016/j.jeurceramsoc.2020.07.001.

[39] J. Ignaczak, L. Zeng, D.F. Sanchez, M. Makowska, K. Górnicka, K. Lankauf, J. Karczewski, P. Jasiński, S. Molin, Fe-modified Mn_2CuO_4 spinel oxides: coatings based on abundant elements for solid oxide cell interconnects, Int. J. Hydrog. Energy (2023), https://doi.org/10.1016/J.IJHYDENE.2023.06.041.

[40] Ł. Mazur, D. Koszelow, M. Zajusz, M. Łapiński, M. Bik, P. Zając, A. Adamczyk, P. Rutkowski, S. Molin, T. Brylewski, Comparison of $Cu_{1.3}Mn_{1.7}O_4$ spinels doped with Ni or Fe and synthesized via wet chemistry and solid-state reaction methods, designed as potential coating materials for metallic interconnects, J. Eur. Ceram. Soc. 43 (2023) 5557–5574, https://doi.org/10.1016/J.JEURCERAMSOC.2023.05.015.

[41] N. Hosseini, M.H. Abbasi, F. Karimzadeh, G.M. Choi, Development of $Cu_{1.3}Mn_{1.7}O_4$ spinel coating on ferritic stainless steel for solid oxide fuel cell interconnects, J. Power Sources 273 (2015) 1073–1083, https://doi.org/10.1016/j.jpowsour.2014.10.017.

[42] B.K. Park, D.W. Kim, R.H. Song, S.B. Lee, T.H. Lim, S.J. Park, C.O. Park, J.W. Lee, Design of a dual-layer ceramic interconnect based on perovskite oxides for segmented-in-series solid oxide fuel cells, J. Power Sources 300 (2015) 318–324, https://doi.org/10.1016/J.JPOWSOUR.2015.09.082.

[43] X. Yang, H. Tu, Q. Yu, Fabrication of Co_3O_4 and $La_{0.6}Sr_{0.4}CoO_{3-\delta}$–$Ce_{0.8}Gd_{0.2}O_{2-\delta}$ dual layer coatings on SUS430 steel by in-situ phase formation for solid oxide fuel cell interconnects, Int. J. Hydrog. Energy 40 (2015) 607–614, https://doi.org/10.1016/J.IJHYDENE.2014.11.021.

[44] T. Brylewski, S. Molin, M. Marczyński, Mazur, K. Domaradzki, O. Kryshtal, A. Gil, Influence of Gd deposition on the oxidation behavior and electrical properties of a layered system consisting of Crofer 22 APU and $MnCo_2O_4$ spinel, Int. J. Hydrog. Energy 46 (2021) 6775–6791, https://doi.org/10.1016/J.IJHYDENE.2020.11.169.

[45] Ł. Mazur, J. Ignaczak, M. Bik, S. Molin, M. Sitarz, T. Aleksander Gil, Brylewski, Effectiveness of a dual surface modification of metallic interconnects for application in energy conversion devices, Int. J. Hydrog. Energy 47 (2022) 6295–6311, https://doi.org/10.1016/j.ijhydene.2021.11.256.

[46] M. Bobruk, K. Durczak, J. Dąbek, T. Brylewski, Structure and electrical properties of Mn-Cu-O spinels, J. Mater. Eng. Perform. 26 (2017) 1598–1604, https://doi.org/10.1007/s11665-017-2588-8.

[47] M. Bobruk, S. Molin, M. Chen, T. Brylewski, P.V. Hendriksen, Sintering of $MnCo_2O_4$ coatings prepared by electrophoretic deposition, Mater. Lett. 213 (2018) 394–398, https://doi.org/10.1016/j.matlet.2017.12.046.

[48] X. Wan, N. Tang, Q. Xie, S. Zhao, C. Zhou, Y. Dai, Y. Yang, A $CuMn_2O_4$ spinel oxide as a superior catalyst for the aerobic oxidation of 5-hydroxymethylfurfural toward 2,5-furandicarboxylic acid in aqueous solvent, Catal. Sci. Technol. 11 (2021) 1497–1509, https://doi.org/10.1039/d0cy01649g.

[49] Y.T. Ting Zhou, Qing Wang Aijuan Xie, Zerui Zhu Xiang Li, Wanqi Zhang, A novel high-performance CeO_2-$CuMn_2O_4$ catalyst for toluene degradation, Environ. Sci. Pollut. Res. Exp. 396 (2020) 22008116.

[50] R. xian Zhou, T. ming Yu, X. yuan Jiang, F. Chen, X. ming Zheng, Temperature-programmed reduction and temperature-programmed desorption studies of CuO/ZrO_2 catalysts, Appl. Surf. Sci. 148 (1999) 263–270, https://doi.org/10.1016/S0169-4332(98)00369-9.

[51] S.D. Robertson, B.D. McNicol, J.H. De Baas, S.C. Kloet, J.W. Jenkins, Determination of reducibility and identification of alloying in copper-nickel-on-silica catalysts by temperature-programmed reduction, J. Catal. 37 (1975) 424–431, https://doi.org/10.1016/0021-9517(75)90179-7.
[52] C.J.G. Van Der Grift, A. Mulder, J.W. Geus, Characterization of silica-supported copper catalysts by means of temperature-programmed reduction, Appl. Catal. 60 (1990) 181–192, https://doi.org/10.1016/S0166-9834(00)82181-8.
[53] M. Shimokawabe, H. Asakawa, N. Takezawa, Characterization of copper/zirconia catalysts prepared by an impregnation method, Appl. Catal. 59 (1990) 45–58, https://doi.org/10.1016/S0166-9834(00)82186-7.
[54] W.P. Dow, Y.P. Wang, T.J. Huang, Yttria-stabilized zirconia supported copper oxide catalyst: I. Effect of oxygen vacancy of support on copper oxide reduction, J. Catal. 160 (1996) 155–170, https://doi.org/10.1006/JCAT.1996.0135.
[55] L. Dong, Z. Liu, Y. Hu, Y. Chen, Dispersion and reduction behavior of systems CuO/α-Fe_2O_3 systems, J. Chem. Soc., Faraday Trans. 94 (1998) 3033–3038, https://doi.org/10.1039/A803630F.
[56] F.C. Buciuman, F. Patcas, T. Hahn, A spillover approach to oxidation catalysis over copper and manganese mixed oxides, Chem. Eng. Process. Process. Intensif. 38 (1999) 563–569, https://doi.org/10.1016/S0255-2701(99)00053-7.
[57] Z. Zhang, Y. Wang, Q. Tan, Z. Zhong, F. Su, Facile solvothermal synthesis of mesoporous manganese ferrite ($MnFe_2O_4$) microspheres as anode materials for lithium-ion batteries, J. Colloid Interface Sci. 398 (2013) 185–192, https://doi.org/10.1016/J.JCIS.2013.01.067.
[58] G. Munteanu, L. Ilieva, D. Andreeva, Kinetic parameters obtained from TPR data for α-Fe_2O_3 and Auα-Fe_2O_3 systems, Thermochim. Acta 291 (1997) 171–177, https://doi.org/10.1016/S0040-6031(96)03097-3.
[59] H. Qin, Y. Yang, W. Shi, Y. She, S. Wu, Heterogeneous Fenton degradation of azithromycin antibiotic in water catalyzed by amino/thiol-functionalized $MnFe_2O_4$ magnetic nanocatalysts, J. Environ. Chem. Eng. 9 (2021) 106184, https://doi.org/10.1016/j.jece.2021.106184.
[60] M. Ghiassee, M. Rezaei, F. Meshkani, S. Mobini, Preparation of the Mn/Co mixed oxide catalysts for low-temperature CO oxidation reaction, Environ. Sci. Pollut. Res. 28 (2021) 379–388, https://doi.org/10.1007/s11356-020-10484-x.
[61] L. Chen, Z. Yang, B. Jha, G. Xia, J.W. Stevenson, Clad metals, roll bonding and their applications for SOFC interconnects, J. Power Sources 152 (2005) 40–45, https://doi.org/10.1016/J.JPOWSOUR.2005.01.055.
[62] A. Petric, H. Ling, Electrical conductivity and thermal expansion of spinels at elevated temperatures, J. Am. Ceram. Soc. 90 (2007) 1515–1520, https://doi.org/10.1111/j.1551-2916.2007.01522.x.
[63] A. Das Sharma, J. Mukhopadhyay, R.N. Basu, Synthesis and characterization of nanocrystalline $MnCo_2O_{4-\delta}$ spinel for protective coating application in SOFC, ECS Trans. 35 (2011) 2509–2517, https://doi.org/10.1149/1.3570249.
[64] B. Talic, V. Venkatachalam, P.V. Hendriksen, R. Kiebach, Comparison of $MnCo_2O_4$ coated Crofer 22H, 441, 430 as interconnects for intermediate-temperature solid oxide fuel cell stacks, J. Alloy. Compd. 821 (2020) 153229, https://doi.org/10.1016/j.jallcom.2019.153229.
[65] B. Pieraggi, CalcUlations of parabolic reaction rate constants, Oxid Met. 27 (1987) 177–185, https://doi.org/10.1007/BF00667057.
[66] J. Karczewski, T. Brylewski, T. Miruszewski, K.B. Andersen, P.Z. Jasinski, S. Molin, High-temperature kinetics study of 430L steel powder oxidized in air at 600–850 °C, Corros. Sci. 149 (2019) 100–107, https://doi.org/10.1016/J.CORSCI.2019.01.005.
[67] B. Talic, V. Venkatachalam, P.V. Hendriksen, R. Kiebach, Comparison of $MnCo_2O_4$ coated Crofer 22H, 441, 430 as interconnects for intermediate-temperature solid oxide fuel cell stacks, J. Alloy. Compd. 821 (2020) 153229, https://doi.org/10.1016/J.JALLCOM.2019.153229.
[68] D. Koszelow, M. Makowska, F. Marone, J. Karczewski, P. Jasiński, S. Molin, High temperature corrosion evaluation and lifetime prediction of porous Fe22Cr stainless steel in air in temperature range 700–900 °C, Corros. Sci. 189 (2021) 109589, https://doi.org/10.1016/J.CORSCI.2021.109589.
[69] H. Shahbaznejad, H. Ebrahimifar, A study on the oxidation and electrical behavior of crofer 22 APU solid oxide fuel cell interconnects with Ni-Co-CeO_2 composite coating, J. Mater. Sci. Mater. Electron. 32 (2021) 7550–7566, https://doi.org/10.1007/s10854-021-05470-z.
[70] A. Weber, E. Ivers-Tiffée, Materials and concepts for solid oxide fuel cells (SOFCs) in stationary and mobile applications, J. Power Sources 127 (2004) 273–283, https://doi.org/10.1016/J.JPOWSOUR.2003.09.024.
[71] Ł. Mazur, S. Molin, J. Dąbek, K. Durczak, M. Pyzalski, T. Brylewski, Physicochemical properties of $Mn_{1.45}Co_{1.45}Cu_{0.1}O_4$ spinel coating deposited on the Crofer 22H ferritic steel and exposed to high-temperature oxidation under thermal cycling conditions, J. Therm. Anal. Calor. 147 (2022) 5649–5666, https://doi.org/10.1007/s10973-021-10884-2.
[72] W. Huang, J.E. Soc, Evaluation of Electrophoretically Deposited $CuMn_{1.8}O_4$ Spinel Coatings on Crofer 22 APU for Solid Oxide Fuel Cell Interconnects Coatings on Crofer 22 APU for Solid Oxide Fuel, Cell (2008).
[73] M. Bednarz, S. Molin, M. Bobruk, M. Stygar, E. Długoń, M. Sitarz, T. Brylewski, High-temperature oxidation of the Crofer 22 H ferritic steel with $Mn_{1.45}Co_{1.45}Fe_{0.1}O_4$ and $Mn_{1.5}Co_{1.5}O_4$ spinel coatings under thermal cycling conditions and its properties, Mater. Chem. Phys. 225 (2019) 227–238, https://doi.org/10.1016/J.MATCHEMPHYS.2018.12.090.
[74] M.J. Reddy, B. Kamecki, B. Talic, E. Zanchi, F. Smeacetto, J.S. Hardy, J.P. Choi, Ł. Mazur, R. Vaßen, S.N. Basu, T. Brylewski, J.-E. Svensson, J. Froitzheimg, Experimental review of the performances of protective coatings for interconnects in solid oxide fuel cells, J. Power Sources 568 (2023) 232831, https://doi.org/10.1016/J.JPOWSOUR.2023.232831.
[75] Z. Zhu, C. Darl-Uzu, U. Pal, S. Gopalan, A.M. Hussain, N. Dale, Y. Fukuyama, Y. Miura, Y. Miyoshi, S. Basu, Comparison of Cu–Mn and Mn–Co spinel coatings for solid oxide fuel cell interconnects, Int. J. Hydrog. Energy 47 (2022) 36953–36963, https://doi.org/10.1016/J.IJHYDENE.2022.08.239.
[76] M. Bik, M. Galetz, J. Dąbrowa, K. Mroczka, P. Zając, A. Gil, P. Jeleń, M. Gawęda, M. Owińska, M. Stygar, M. Zajusz, J. Wyrwa, M. Sitarz, Polymer derived ceramics based on SiAlOC glasses as novel protective coatings for ferritic steel, Appl. Surf. Sci. 576 (2022) 151826, https://doi.org/10.1016/j.apsusc.2021.151826.
[77] J. Mougin, T. Le Bihan, G. Lucazeau, High-pressure study of Cr_2O_3 obtained by high-temperature oxidation by X-ray diffraction and Raman spectroscopy, J. Phys. Chem. Solids 62 (2001) 553–563, https://doi.org/10.1016/S0022-3697(00)00215-8.
[78] R.L. Farrow, P.L. Mattern, A.S. Nagelberg, Characterization of surface oxides by Raman spectroscopy, Appl. Phys. Lett. 36 (1980) 1529–1542, https://doi.org/10.1063/1.91429.
[79] H.D. Lutz, B. Müller, H.J. Steiner, Lattice vibration spectra. LIX. Single crystal infrared and Raman studies of spinel type oxides, J. Solid State Chem. 90 (1991) 54–60, https://doi.org/10.1016/0022-4596(91)90171-D.
[80] T.Van Everbroeck, R.G. Ciocarlan, W.Van Hoey, M. Mertens, P. Cool, Copper-containing mixed metal oxides (Al, Fe, Mn) for application in three-way catalysis, Catalysts 10 (2020) 1–20, https://doi.org/10.3390/catal10111344.
[81] C.M. Julien, M. Massot, C. Poinsignon, Lattice vibrations of manganese oxides: Part I. Periodic structures, Spectrochim. Acta - Part A Mol. Biomol. Spectrosc. 60 (2004) 689–700, https://doi.org/10.1016/S1386-1425(03)00279-8.
[82] G. Zhou, X. Gu, W. Xie, T. Gao, J. Peng, X.S. Wu, Polarized Raman scattering studies of hexagonal $YMnO_3$ single crystal, IEEE Trans. Magn. 51 (2015), https://doi.org/10.1109/TMAG.2015.2438154.
[83] S. Mahana, S.K. Pandey, B. Rakshit, P. Nandi, R. Basu, S. Dhara, S. Turchini, N. Zema, U. Manju, S.D. Mahanti, D. Topwal, Site substitution in $GdMnO_3$: effects on structural, electronic, and magnetic properties, Phys. Rev. B 102 (2020), https://doi.org/10.1103/PhysRevB.102.245120.
[84] S. Chevalier, J.P. Larpin, Formation of perovskite type phases during the high temperature oxidation of stainless steels coated with reactive element oxides, Acta Mater. 50 (2002) 3107–3116, https://doi.org/10.1016/s1359-6454(02)00106-4.
[85] S. Molin, H. Persson, T.L. Skafte, A.L. Smitshuysen, S.H. Jensen, K.B. Andersen, H. Xu, M. Chen, P.V. Hendriksen, Effective yttrium based coating for steel interconnects of solid oxide cells: corrosion evaluation in steam-hydrogen atmosphere, J. Power Sources 440 (2019), https://doi.org/10.1016/j.jpowsour.2019.226814.
[86] E. Tondo, M. Boniardi, D. Cannoletta, M.F. De Riccardis, B. Bozzini, Electrodeposition of yttria/cobalt oxide and yttria/gold coatings onto ferritic stainless steel for SOFC interconnects, J. Power Sources 195 (2010) 4772–4778, https://doi.org/10.1016/j.jpowsour.2010.02.055.
[87] M. Grioni, J.B. Goedkoop, R. Schoorl, F.M.F. de Groot, J.C. Fuggle, F. Schäfers, E. E. Koch, G. Rossi, J.-M. Esteva, R.C. Karnatak, Studies of copper valence states with Cu L 3 x-ray-absorption spectroscopy, Phys. Rev. B 39 (1989) 1541–1545. ⟨https://link.aps.org/doi/10.1103/PhysRevB.39.1541⟩.
[88] S. Gautam, S. Muthurani, M. Balaji, P. Thakur, D.P. Padiyan, K.H. Chae, S.S. Kim, K. Asokan, Electronic structure studies of nanoferrite $Cu_xCo_{1-x}Fe_2O_4$ by X-ray absorption spectroscopy, J. Nanosci. Nanotechnol. (2011), https://doi.org/10.1166/jnn.2011.3249.
[89] J. Kang, G. Kim, H.J. Lee, D.H. Kim, H.S. Kim, J.H. Shim, S. Lee, H. Lee, J. Kim, B. H. Kim, B.I. Min, Soft x-ray absorption spectroscopy and magnetic circular dichroism study of the valence and spin states in spinel $MnFe_2O_4$, Phys. Rev. B (2008) 3–7, https://doi.org/10.1103/PhysRevB.77.035121.